Composites: Part A 186 (2024) 108386

Contents lists available at ScienceDirect

Composites Part A

journal homepage: www.elsevier.com/locate/compositesa

An analytical model for wrinkle-free forming of composite laminates

Alex Trenam [a,*], Chrysoula Aza [b], Christian Jones [b], Guy Lawrence [c], Lee Harper [c], Andrew Rhead [b,d], Evripides G. Loukaides [b,e], Richard Butler [b,d]

[a] Institute for Mathematical Innovation, University of Bath, Bath, BA2 7AY, UK
[b] Department of Mechanical Engineering, University of Bath, Bath, BA2 7AY, UK
[c] Composites Research Group, Faculty of Engineering, University of Nottingham, Nottingham, NG7 2RD, UK
[d] Centre for Integrated Materials, Processes and Structures
[e] Centre for Digital Manufacturing and Design

ARTICLE INFO

Keywords:
A. Laminates
B. Defects
C. Analytical modelling
E. Forming

ABSTRACT

Double Diaphragm Forming (DDF) of 3D shapes significantly increases production rates for laminated composite parts when compared with Automated Fibre Placement. However, it is prone to the occurrence of wrinkling defects, which can lead either to concession of part strength or expensive and wasteful part scrappage. Finite element simulation of the process is computationally costly and not suited to preliminary design for manufacture. In this work a novel analytical model is presented, based on obtaining the wrinkle profile via energy minimisation using a Rayleigh–Ritz approach, which enables rapid mechanics-based assessment of formability for the design of wrinkle-free composite products. The new modelling approach is validated against eight experimental DDF forming trials performed over C-shaped tools with double curvature using both dry Non-Crimped Fabric and unidirectional prepreg material. The model successfully predicts the three cases for which wrinkling is absent and the five cases where it occurs.

1. Introduction

A prominent preforming process which has been adopted by industry is Double Diaphragm Forming (DDF). In DDF the laminate is enclosed between two elastomer diaphragms, within which a vacuum is created to consolidate the plies under atmospheric pressure in the out-of-plane direction. Both the diaphragms and the laminate are then placed against a tool surface, and a second vacuum draws the bottom diaphragm down under atmospheric pressure to conform the laminate to the tool geometry. In the case of non-crimp fabrics (NCF), the binder is then activated by heat and the part cooled before releasing pressure. Uni-directional fibre laminates pre-impregnated with resin (UD prepregs) are formed at elevated temperature using DDF, to ensure that resistance to inter-layer slip is minimised. DDF of NCF and UD prepreg can achieve much higher production rates than Automated Fibre Placement (AFP) over 3D part geometry, and significantly lowers the capital cost for large scale production compared to matched tool forming. It is, however, more susceptible to defect formation and cannot equal the local forming control of hand layup. Defects typically emerge when the in-plane stress conditions cause the material to wrinkle.

The preforming process is preceded by the cutting of the plies to shape to create the blank. Then some DDF machines actuate the blank towards the tool by moving the frames that hold the two membranes and other machines actuate the tool instead. In both scenarios, the areas of the tool that typically make first contact with the bottom membrane are the "tallest" ones in the blank through-thickness direction (the z-direction in Fig. 1). Depending on the geometry of the tool, the location of first contact influences the ability of the material to conform to the shape. A typical forming setup is shown in Fig. 1. This interaction can be influenced to a certain extend by the introduction of risers on the forming bed, Chen et al. [1]. Additional methods which have been considered to improve NCF formability include: removing some of the stitching on the NCF, Chen et al. [2]; lubrication, Yu et al. [3]; constraining the material locally with distributed magnetic clamps, Jagpal et al. [4], and more. These interventions represent additional challenges in efforts to predictively model the outcome of forming attempts. A further formability parameter is the relative orientation of different plies within a stack. Plies of the same orientation deform in the same manner so the relative motion is negligible, see [5,6]. However, for plies of differing orientations this is not the case, and defects such as laddering, bridging, and wrinkling, which can reduce the mechanical properties of the final part, see [7,8], can arise as a result, Johnson et al. [9]. These should not be tolerated in a production environment and remain an obstacle for designers and production engineers who

---

* Corresponding author.
E-mail addresses: amt83@bath.ac.uk (A. Trenam), R.Butler@bath.ac.uk (R. Butler).

https://doi.org/10.1016/j.compositesa.2024.108386
Received 9 April 2024; Received in revised form 23 July 2024; Accepted 31 July 2024

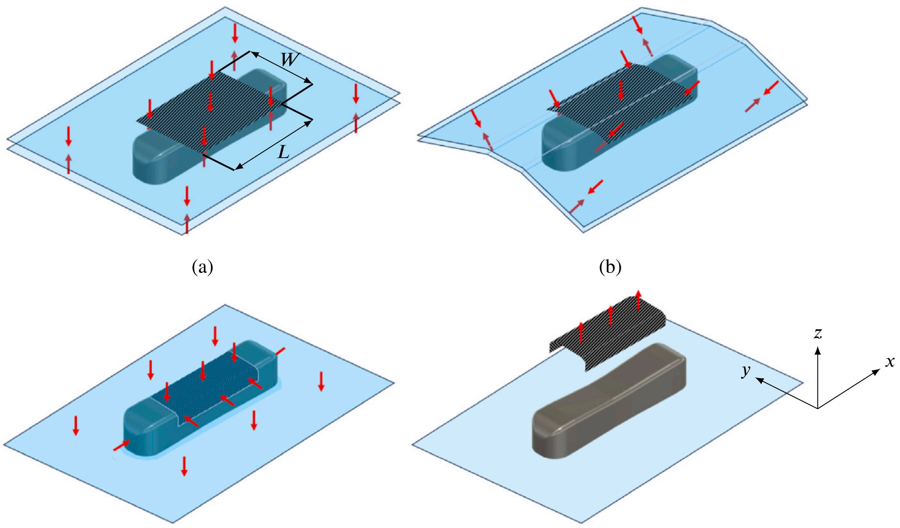

(a) (b)

(c) (d)

Fig. 1. The Double Diaphragm Forming process: (a) the blank is first consolidated between the double diaphragm under vacuum pressure before (b) being lowered over the tool geometry, which it is (c) drawn towards and further consolidated by a second vacuum. After undergoing a curing process, (d) the finished spar is removed from the tool. The part shown is a doubly-curved C-spar with part axes x, y, and z. The blank has length L and width W.

either have to rely on expensive trial-and-error testing or have to wait for slow and challenging FEA simulations.

Three-dimensional finite element analysis can provide solutions which have a high correspondence to experimentally observed results. For example, complex behaviours such as the transition between squeezing and bleeding resin flow in the compaction of uncured prepreg systems can be effectively captured, see [10,11]. However, the temporal and computational costs associated with solving the arising systems of partial differential equations can be very large. Physically-consistent modelling simplifications, such as the use of shell finite elements, reduce the computational complexity whilst preserving the key behaviours of the system, see [12–15]. Despite this, they still require significant computation time, in the order of hours and days, for reliable results. Given the complexity of the material system and the non-linearity introduced by typical part geometries, several simplifications have to be made to allow for a fast, tractable model. A rapid assessment of the feasibility of a part would allow designers to iterate through options without significant investment of time and resources, and leave more detailed analysis to a narrow range of candidate design parameters. Although the formability of laminates can be improved by minimising the number of slip interfaces between layers, where incompatibility between neighbouring plies leads to slippage, as shown in [9], it is demonstrated in [16] that wrinkles can occur in long, apparently formable, parts because long fibres restrain slip.

In this paper, we present a new analytical model to predict the conditions for which wrinkles cannot dissipate due to this slip-constraining length effect. The method focuses on wrinkling as a result of the initial forming process and does not account for consolidation-induced defects. Detailed experimental and numerical studies in this direction have been conducted in, for example, Thompson et al. [17] and Rashidi et al. [18]. The approach proposed in this work emphasises speed, allowing designers to quickly reject infeasible geometries or ply stacking sequences.

The model is validated against multi-layer forming trials (experiments) using both NCF and UD prepreg material. It is focused on predicting the appearance of transverse wrinkles in DDF of multi-ply laminates over a C-spar tool geometry featuring complex (double) curvature. This geometry is chosen since it is challenging to form without wrinkling and is typically used in the manufacturing of components for aerospace wing applications. The emergence of wrinkles with this C-spar geometry has also been linked to the length of fibres for prepreg single-diaphragm forming, Scarth et al. [16]. The speed of the proposed method improves the capability of iterating through design parameters and could lead to increased rates of defect-free production, allowing more layers to be formed simultaneously without scrappage or concession of parts.

2. Methodology overview and notation

2.1. Model aims, assumptions, and physical context

The model is centred on the kinematics of deformation for a flat rectangular blank that is deformed into a symmetric recess, as shown in Fig. 1, and we separate our approach into two stages: (i) the formation of wrinkles during the forming process; and (ii) the (potential) dissipation of the formed wrinkles through consolidation. Wrinkling arises due to forming the laminate at the top of the ramp, which leads to an excess of material away from the tool face, in the centre of the recess. Note that it is the forming of doubly-curved (shell-like) shapes which necessitates in-plane deformation of the blank, triggering slip between misaligned layers. A one-dimensional approximation is used because we assume that the wrinkle is wide compared with its wavelength, as has been observed experimentally, Scarth et al. [16], Johnson et al. [9] and Lawrence et al. [19].

By adopting a macroscale perspective the model aims to produce very fast predictions of whether or not a wrinkle will be present at the end of the forming operation. Simplifying assumptions, which constrain the tool geometry and wrinkle shape, allow for an analytic description of the work required in the deformation of the blank. A constrained minimisation of the corresponding energy expressions can then provide quantitative solutions for a range of process and material parameters. The inputs available for exploration include (but are not limited to) the local ramp angles on the tool that direct the extent of deformation, the through-thickness consolidation stiffness of the material, the compatibility of in-plane ply deformation and the friction between plies, the number of plies and their bending stiffness and orientation.

The deformation of the blank begins when it meets the top corners of the tool geometry on either side of the yz-plane of mid-length symmetry in Fig. 1. The through-thickness shearing of the blank results in inter-ply slipping and the generation of a bookend, where end shortening varies from ply to ply, at either end since the fibres are subject to small forming stresses and considered inextensible (see Fig. 2(a)). When

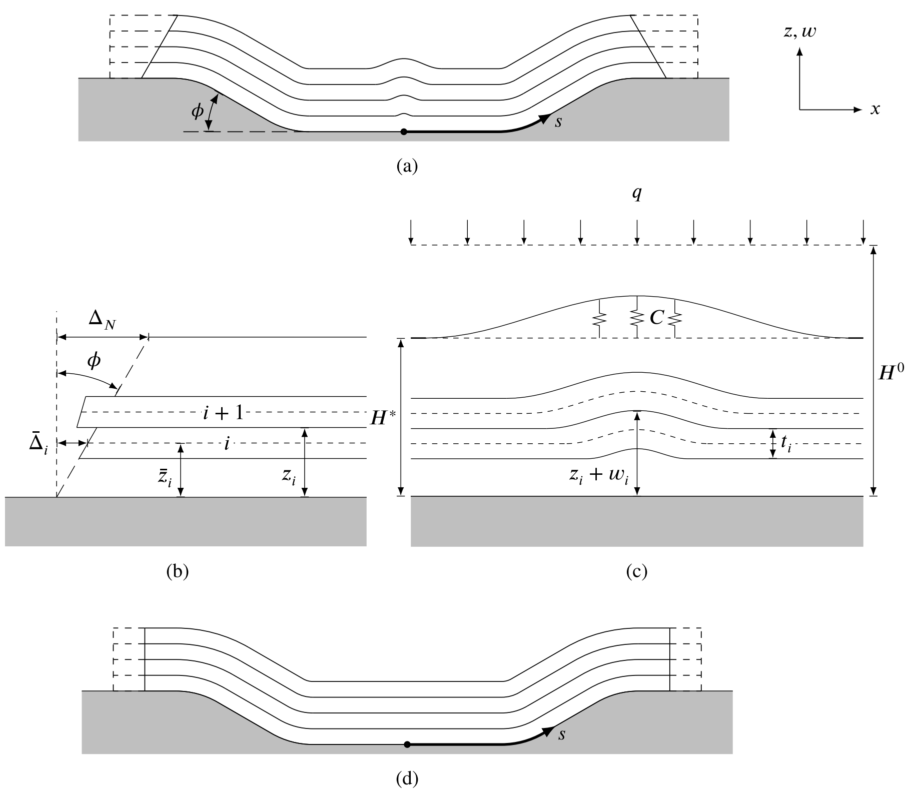

(a)

(b)

(c)

(d)

Fig. 2. Sectional view (in the xz-plane) of Fig. 1(c), showing the two-step modelling process and notation for the forming of the C-spar geometry. (a) A wrinkle is created as a result of first forming the outer (convex) corners, followed by the inner (concave) corners. (d) It is then dissipated if the part is formable. Depicted in (b) is the ply slip at the bookend between plies i and $i+1$ of different fibre orientation, and (c) shows the geometry of the wrinkle.

plies are aligned with each other the bookend is linear; neighbouring plies of differing orientations give rise to discontinuous bookends (see Fig. 2(b)). As a consequence of this bookend, the plies experience compression at the plane of symmetry, which increases further away from the surface of the tool. For sufficiently large compression in this first stage of deformation, fibres buckle out of plane and wrinkles appear with a range of amplitudes and wavelengths.

At this point in the deformation timeline, the ply stack is in contact with the tool across its length and the pressure is compressing the emerging wrinkles. During the second stage of deformation, the local instability can be dissipated if misaligned plies are capable of sliding with respect to the plies above and below them. The dissipation of the wrinkles is therefore determined by the friction between plies, the forming pressure and the geometry of the part. The role of ply orientation and inter-ply friction on the size of wrinkles is significant and has been discussed by many authors, e.g. [20,21]. Similarly, the degree of consolidation of the material has an impact on the frictional behaviour, and in turn on the formability. At the microscale this relates to changes to the surface topography and depends on applied pressure and fibre orientation, Lawrence et al. [21].

Additional complications are introduced by the dependence of bending stiffness on the curvature of the deformed laminate and on the orientation of the fibres with respect to the target geometry. In [13] it was observed that the bending stiffness is greater than the sum of the stiffnesses of individual plies in the laminate stack, with this difference being attributed to the frictional moment between plies in regions of curvature. This was further demonstrated in [21], where both the bending stiffness and shear stiffness were shown to increase as a result of inter-ply friction. It has been suggested that transverse wrinkles, which are observed occurring perpendicular to the applied bending in the centre of the C-spar, are a result of the inter-ply friction since they do not appear in the case of a single ply, Yu et al. [20], or multiple aligned plies.

In Sections 2.2 and 2.3 a general wrinkle profile is presented, however, the implementation of our model is limited to instances of a symmetric group of wrinkles with fixed amplitude (integer periods of a cosine wave) at the centre of the tool. The localisation of the calculation to only a single group of wrinkles, along with simplifying assumptions discussed below, allows the problem to be reduced to solving one nonlinear equation (31) for the wrinkle formation (Section 3) and one linear equation (35) for their (potential) dissipation (Section 4), drastically cutting analysis times. The reduced complexity allows results to be calculated for a range of parameter values in seconds without the need for specialist hardware/software (i.e. high performance computing). The results in Section 5 demonstrate that this is sufficient to correctly predict wrinkling in agreement with reality, but detailed simulations and physical experiments would need to be completed to further investigate laminate forming configurations prior to production.

The model assumes that each ply is inextensible in its fibre direction(s), meaning we can neglect in-plane elastic energy. This remains the case for NCF plies since the extensible deformation is treated as plastic. The plies are assumed to wrinkle as one, i.e. delamination is not allowed, and consolidation of plies must be globally uniform, with a local exception in the region of the wrinkles. The deformation is assumed to occur slowly, thus removing any dynamic effects. The interface between the tool and the bottom diaphragm is assumed to be smooth and frictionless, and the diaphragms are assumed to not restrain in-plane ply deformation. The wrinkles are taken to be symmetric (i.e. not skewed to one side) and to form in the centre of the recess due to the symmetry of the part.

2.2. Overview of the wrinkling model

We consider a one-dimensional model of an N-ply laminate stack being formed over a C-spar geometry, as depicted in Fig. 2, which shows a sectional view of the forming setup in the xz-plane. The origin is located at the centre of the recess, with the yz-plane of symmetry from Fig. 1 reduced to symmetry about the z-axis at $s = 0$, where s parameterises the arc length of the tool surface.

The blank has a fixed length L and width W, as shown in Fig. 1(a). The "height" (orthogonal to the tool geometry) of the midplane of the ith ply in the stack is denoted by $\bar{z}_i + \bar{w}_i$, where $\bar{z}_i$ is a constant value associated to the initial consolidation of the laminate, and $\bar{w}_i = \bar{w}_i(s)$ captures spatially-dependent deviations about this baseline. We take the convention that $\bar{z}_1 + \bar{w}_1$ represents the midplane of the ply in contact with the tool surface, and $\bar{z}_N + \bar{w}_N$ represents the midplane of the ply at the top of the N-ply stack. The interface between the ith ply and $(i+1)$ th ply is denoted by $z_i + w_i$. In addition to inter-ply interfaces, we use this notation to refer to the free surface at the top of the laminate stack $z_N + w_N$ and the interface between the bottom ply and the tool surface $z_0 + w_0$. The symbol H^0 represents the total laminate thickness at the initial time before uniform consolidation, and H^* is the value when uniformly consolidated by pressure q. This notation is shown in Fig. 2(c), and the same superscripts are used with individual ply thicknesses t_i.

The first stage of the modelling process, discussed in Section 3, is an energy minimisation to determine the most energetically favourable wrinkle profile if wrinkling were to occur. The laminate is assumed to be uniformly consolidated up to the initial onset of wrinkling, and we consider variations about this state through the relative energy per unit width

$$U_1 = \underbrace{U_{\mathrm{C}}\left(w_N\right)}_{\substack{\text{consolidation}\\ \text{deviation}}} + \sum_{i=1}^{N}\Big(\underbrace{U_{\mathrm{B}}\left(\bar{w}_i\right)}_{\text{bending}} + \underbrace{U_{\mathrm{F_W}}\left(\bar{w}_i\right)}_{\substack{\text{in-wrinkle}\\ \text{friction}}}\Big), \tag{1}$$

where U_{C} refers to deviations from the initial consolidation energy caused by wrinkling, U_{B} is the stored bending energy in the plies, and $U_{\mathrm{F_W}}$ is the non-conservative frictional energy attributed to inter-ply slip due to curvature. Each of these terms works to oppose wrinkle formation, however, the assumed inextensibility of the fibres, along with the imposition of a prescribed bookend angle (discussed in more detail in Section 2.3), constrains the solution to be non-trivial in general.

In the second step, which is the focus of Section 4, we examine the energy required to dissipate the wrinkles generated above by considering the relative energy per unit width

$$U_2 = \underbrace{U_{\mathrm{C}}\left(w_N\right)}_{\substack{\text{consolidation}\\ \text{deviation}}} + \sum_{i=1}^{N}\Big(\underbrace{U_{\mathrm{B}}\left(\bar{w}_i\right)}_{\text{bending}} - \underbrace{U_{\mathrm{F_W}}\left(\bar{w}_i\right)}_{\substack{\text{in-wrinkle}\\ \text{friction}}}\Big) - \lambda \sum_{i=1}^{N-1}\Big(\underbrace{U_{\mathrm{F_P}}\left(w_i\right)}_{\substack{\text{in-plane}\\ \text{friction}}}\Big), \tag{2}$$

where the first three terms on the right-hand side are the same as before (noting the sign change for $U_{\mathrm{F_W}}$, since friction now acts to oppose wrinkle dissipation), and $U_{\mathrm{F_P}}$ refers to the inter-ply friction along the length of the part outside regions of wrinkling. Setting $U_2 = 0$, which balances the energies sustaining the wrinkles and dissipating them, and rearranging to obtain the critical condition

$$\lambda = \frac{U_{\mathrm{C}}\left(w_N\right) + \sum_{i=1}^{N}\left(U_{\mathrm{B}}\left(\bar{w}_i\right) - U_{\mathrm{F_W}}\left(\bar{w}_i\right)\right)}{\sum_{i=1}^{N-1}\left(U_{\mathrm{F_P}}\left(w_i\right)\right)} \tag{3}$$

allows one to determine the value of the blank size scaling factor λ. If $\lambda < 1$ the in-plane frictional energy exceeds the other energies and permanent wrinkling is predicted, and if $\lambda > 1$ the opposite case is expected and the blank size could be increased. At the critical value $\lambda = 1$ the energies are balanced. One may view Eq. (3) as an expression of the formability of the part as a function of the design parameters, and so comparing values of λ for different parameter choices can be used to inform early-stage design decisions.

2.3. Bookend geometry and ply compatibility

Following the forming kinematics, the bookend profile is considered in two phases. As demonstrated in Fig. 2(b), the symbol Δ_i is used to denote the distance the end of the ith interface slips relative to the interface with the tool surface. Similarly, the symbol $\bar{\Delta}_i$ denotes the distance the end of the ith midplane slips relative to the interface with the tool surface. We capture the impact of the tool geometry in our framework by directly relating the bookend to the ramp angle ϕ (measured in radians).

During the wrinkle formation stage it is assumed that the outer (convex) corners, which occur first in the forming process, are formed without issue and generate an associated linear bookend in the neighbourhood of the wrinkles, as shown in Fig. 2(a). This is expressed for the midplanes as

$$\bar{\Delta}_i = \bar{z}_i \phi, \tag{4}$$

and an analogous equation holds at the interfaces.

The bookend profile at the ends of the plies is determined in the second stage of the process (wrinkle dissipation) by the compatibility of neighbouring plies in the stacking sequence, which governs whether or not the plies are able to deform in the same manner. Multiple plies of the same orientation are formable within the limits of ply shear deformation. In this case, no inter-ply slip occurs. Laminates with plies of different orientations can only form if inter-ply slip is permitted. The compatibility of deformation modes of adjacent plies is a value between −1 and 1, which refers to how easy it is for the plies to deform together in the same manner, and was introduced in [9] for unidirectional plies. For example, a stack of plies with the same orientation is fully compatible and as a result are able to shear as one. Inherently this depends on the relative orientation of the plies in question. A compatibility of 0 indicates incompatible modes of deformation, such as shearing in opposite directions at the same time, and a compatibility of 1 or −1 (a sign change indicating a change in deformation direction) means that the modes are completely compatible, and the plies undergo the same deformation.

The orientation of the fibres in the ith ply is given by $\theta_i \in (-90, 90]$, where the angle is measured relative to the longitudinal x-axis of the C-spar (see Fig. 3, which is discussed below). In the bi-axial case we write θF to refer to a bi-axial NCF ply with θ° bottom fibres and $(90-\theta)^\circ$ top fibres. This notation emphasises the compatibility of bi-axial plies with the same fibre directions (e.g. a stack of 0°/90° plies, denoted 0F, or a stack of ±45° plies, denoted 45F, bi-axial plies), which are able to deform together, and allows us to present a unified treatment of prepreg and bi-axial plies, where the former are denoted as θ, i.e. without F.

Fig. 3 shows the pure deformation modes for a 0F bi-axial ply (c.f. Figure 1 in [9], which shows the deformation modes for a prepreg ply). The first two modes correspond to deformations along the 0° and 90° fibre directions, respectively, and are relatively high-energy modes due to the large axial stiffness of the fibres. The system will naturally seek low energy modes in order to find a minimum energy state, which are represented by modes of deformation that do not require fibre extension. The third deformation mode is ply shearing, which is a relatively low-energy mode. Excessive compression in fibre modes I and II tends to result in out-of-plane wrinkling due to the high-energy nature of the modes, and as such it is these modes which are of most interest. Further, in the one-dimensional context, we only see deformation in the 0° direction so we can neglect fibre mode II and focus solely on the compatibility of fibre mode I.

The (potentially discontinuous) profile of the bookend is governed by the orientation of the plies, which enters as a standard two-dimensional strain transformation of the fibre mode I deformation from the fibre axis to the part axis x. Each ply has an associated upper interface bookend Δ_i^U and lower interface bookend Δ_i^L, defined by

$$\Delta_i^U = z_i \phi \cos^2\left(\theta_i\right), \tag{5}$$

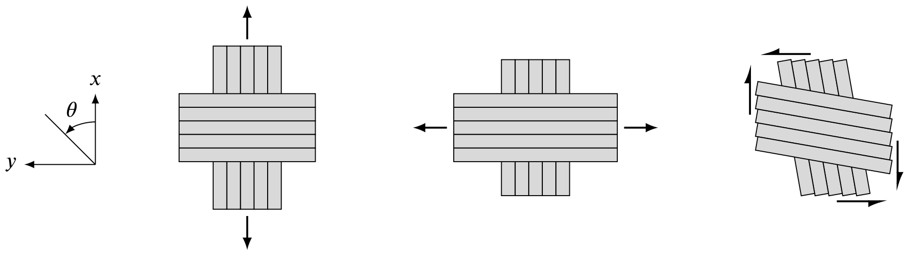

(a) Fibre mode I (b) Fibre mode II (c) Shear mode

Fig. 3. The pure deformation modes of a bi-axial ply. In the case of UD prepreg, the modes shown in (b) and (c) are resin-dominated, see Figure 1 in [9].

$$\Delta_i^L = z_{i-1}\phi\cos^2\left(\theta_i\right), \tag{6}$$

determining the individual ply bookend as a consequence of intra-ply shearing. The impact of neighbouring ply compatibility, and the resulting inter-ply slip, is expressed through the discrepancy between upper and lower interface bookends in contact. A linear bookend is then recovered when $\Delta_i^U = \Delta_{i+1}^L$, which occurs for completely compatible deformation modes in the ith and $(i+1)$th plies. At the midplanes the bookend is given by

$$\bar{\Delta}_i = \bar{z}_i\phi\cos^2\left(\theta_i\right). \tag{7}$$

We emphasise that Eqs. (4)–(7) are calculable a priori as long as the uniformly consolidated ply thicknesses t_i^* are known, since we have

$$\bar{z}_i = \sum_{j=1}^{i}\left(t_j^*\right) - \frac{1}{2}t_i^*, z_i = \sum_{j=1}^{i}\left(t_j^*\right). \tag{8}$$

The prescribed bookend fixes the domains (intervals over which input values are taken) of $\bar{w}_i$ and w_i, which are given by $\bar{\ell}_i = \left[-\frac{1}{2}L + \bar{\Delta}_i, \frac{1}{2}L - \bar{\Delta}_i\right]$ and $\ell_i = \left[-\frac{1}{2}L + \Delta_i, \frac{1}{2}L - \Delta_i\right]$, respectively. These domains capture the end shortening of the plies and are important for ensuring the correct inextensibility condition is obtained. For instance, if there was no bookend all of the domains would simply be the length of the blank $\left[-\frac{1}{2}L, \frac{1}{2}L\right]$. As a consequence of the assumption that the fibres are inextensible, any bookending caused by the geometry must be taken up as wrinkling. This condition is formulated in terms of the arc length of the ply midplanes as

$$2\bar{\Delta}_i = \int_{\bar{\ell}_i}\left(\sqrt{1+\left(\frac{\partial\bar{w}_i}{\partial s}\right)^2} - 1\right)ds, \tag{9}$$

where the slip distance is doubled to account for the symmetry of the geometry.

3. Wrinkle formation

In this section we examine each of the terms on the right-hand side of Eq. (1) and follow through the energy minimisation process. We state the general theory, before assuming a particular wrinkle profile in order to obtain a closed-form solution.

We begin with the consolidation deviation energy U_{C}, which is defined to be the difference between the compressive energy stored in the laminate in its uniformly consolidated state and its wrinkled state. As in [22], the non-linear stress–strain relationship between the applied consolidation pressure q and the change in laminate thickness $H - H^0$ is modelled as quadratic, expressed as

$$q(H) = C\left(\frac{H^0 - H}{H^0}\right)^2, \tag{10}$$

where C is the out-of-plane compaction stiffness of the laminate. We consider perturbations of the laminate compaction around the initial uniform consolidation by approximating small variations as linear, with the magnitude of the gradient given (since $H^0 > H^*$) by

$$\left|\frac{dq}{dH}\left(H^*\right)\right| = \frac{2C\left(H^0 - H^*\right)}{\left(H^0\right)^2}. \tag{11}$$

One may view the uniformly consolidated laminate as being like a spring system which resists deviations away from its neutral position, with the spring constant given by Eq. (11). From this perspective, we define the consolidation deviation energy to be

$$U_{\mathrm{C}}\left(w_N\right) = \int_{\ell_N}\left(\frac{C\left(H^0 - H^*\right)}{\left(H^0\right)^2}w_N^2\right)ds. \tag{12}$$

The second term in Eq. (1) accounts for the stored bending energy in each of the plies as a result of wrinkling. Each ply has an anisotropic bending response, with the bending stiffness of the ith ply in the direction of wrinkling (in the x-direction), denoted D_i, depending on the principal fibre direction (or orientation) of the ply relative to the imposed bending force. We make use of Krenchel's approximation, see [23], to estimate the bending stiffness for bi-axial plies where, for component layers indexed by i_1 and i_2, the combined bi-axial bending stiffness of the ith ply is given by

$$D_i = D_{i_1}\cos^4\theta_{i_1} + D_{i_2}\cos^4\theta_{i_2}. \tag{13}$$

We then define the bending energy

$$U_{\mathrm{B}}\left(\bar{w}_i\right) = \int_{\bar{\ell}_i}\left(\frac{1}{2}D_i\left|\kappa\left(\bar{w}_i\right)\right|^2\right)ds, \tag{14}$$

where $\kappa\left(\bar{w}_i\right)$ is the curvature of $\bar{w}_i$, which, for $\frac{\partial\bar{w}_i}{\partial s} \ll 1$ (i.e. for wrinkles with much greater wavelength than amplitude), can be approximated using Taylor's theorem to obtain

$$\kappa\left(\bar{w}_i\right) \approx \frac{\partial^2\bar{w}_i}{\partial s^2}. \tag{15}$$

We emphasise that, since s parameterises the arc length of the tool surface, only curvature due to wrinkling (and not the tool geometry) enters into the calculation. Under the same conditions ($\frac{\partial\bar{w}_i}{\partial s} \ll 1$), one can make the Taylor approximation

$$\sqrt{1+\left(\frac{\partial\bar{w}_i}{\partial s}\right)^2} - 1 \approx \frac{1}{2}\left(\frac{\partial\bar{w}_i}{\partial s}\right)^2, \tag{16}$$

which will, after specifying the wrinkle shape function in Section 3.1, allow us to explicitly treat terms containing arc length.

The final term in Eq. (1) concerns the energy lost to friction through inter-ply slip, induced by the incompatibility of tensile and compressive surfaces of neighbouring plies as a result of the curvature of wrinkling, following experimental evidence, Liang et al. [13]. The coefficient of friction at the interface between the ith and $(i+1)$th plies is given by μ_i, where the tool surface is assumed smooth, and we neglect friction at the free surface (so $\mu_0 = \mu_N = 0$). The frictional moment per unit area M_f about the ith midplane $\bar{w}_i$ is defined by

$$M_f\left(\bar{w}_i\right) = \frac{\mu_i + \mu_{i-1}}{2}qt_i^*. \tag{17}$$

The in-wrinkle frictional energy is then given by

$$U_{\mathrm{Fw}}\left(\bar{w}_i\right) = \int_{\bar{\ell}_i} \left(K_i M_f\left(\bar{w}_i\right)\left|\kappa\left(\bar{w}_i\right)\right|\right) ds, \tag{18}$$

where K_i is the total length of all intervals in $\bar{\ell}_i$ upon which $\bar{w}_i$ has non-zero curvature.

3.1. Choice of wrinkle shape function

If a detailed and accurate modelling solution is the priority, one would typically adopt the approach of the calculus of variations to derive the governing system of partial differential equations from the associated system energy. The resulting equations for the problem in question would typically involve the coupled non-linear fourth-order elasticity equations, which are both challenging and computationally expensive to solve. Alternatively, each of the energies defined in the previous section can be explicitly calculated by imposing a particular form of the wrinkles. In the terminology of the Rayleigh–Ritz method, we make a specific choice of shape function and seek the minimiser of the energy among the resulting set of admissible functions. Following this approach we are able to obtain a closed-form solution to the complex problem we seek to model.

Based on observed data, Johnson et al. [9], we define

$$\bar{w}_i(s) = \begin{cases} \bar{A}_i\left(1+\cos\left(\frac{n\pi s}{\bar{\xi}_i}\right)\right), & s \in \left[-\bar{\xi}_i, \bar{\xi}_i\right], \\ 0, & \text{otherwise}, \end{cases} \tag{19}$$

where $\bar{A}_i$ and $\bar{\xi}_i$ are the midplane half-amplitudes and the total half-wavelengths, respectively. This equates to assuming n wrinkles form in the middle of the central recess, each with the shape of a single period of a cosine wave of half-amplitude $\bar{A}_i$ and half-wavelength $\hat{\bar{\xi}}_i = \bar{\xi}_i/n$. The interfaces are defined analogously, with A_i and ξ_i representing the interface half-amplitudes and total half-wavelengths, with $\hat{\xi}_i = \xi_i/n$ giving the individual wrinkle half-wavelengths. Experimental results suggest a decay in wrinkle amplitude through the thickness of the laminate, Johnson et al. [9], with the greatest amplitude seen in the top ply. In particular, we can write all half-amplitudes in terms of $\bar{A}_N$ since, for any i, we assume the relations

$$\bar{A}_i = \frac{\bar{z}_i}{\bar{z}_N}\bar{A}_N, \quad A_i = \frac{z_i}{\bar{z}_N}\bar{A}_N. \tag{20}$$

Combining the assumed midplane profile of Eq. (19) and the arc length approximation of Eq. (16) with Eq. (9) gives

$$2\bar{\Delta}_i \approx \frac{\bar{A}_i^2 n^2\pi^2}{\bar{\xi}_i^2}\int_0^{\bar{\xi}_i}\left(\sin^2\left(\frac{\pi s}{\bar{\xi}_i}\right)\right) ds = \frac{\bar{A}_i^2 n^2\pi^2}{2\bar{\xi}_i}. \tag{21}$$

In other words, the half-amplitudes can be expressed in terms of the total half-wavelengths and the bookend-induced slippage as

$$\bar{A}_i \approx \frac{2\sqrt{\bar{\xi}_i\bar{\Delta}_i}}{n\pi}. \tag{22}$$

In combination with Eq. (20), this yields

$$\bar{\xi}_i \approx \frac{\bar{A}_i^2 n^2\pi^2}{4\bar{\Delta}_i} = \left(\frac{\bar{z}_i}{\bar{z}_N}\right)^2\frac{\bar{A}_N^2 n^2\pi^2}{4\bar{\Delta}_i} \approx \frac{\bar{\Delta}_N}{\bar{\Delta}_i}\left(\frac{\bar{z}_i}{\bar{z}_N}\right)^2\bar{\xi}_N = \frac{\bar{z}_i}{\bar{z}_N}\bar{\xi}_N, \tag{23}$$

where the final equality is a consequence of Eq. (4). Similarly, for the ply interfaces we have

$$A_i \approx \frac{2\sqrt{\xi_i\Delta_i}}{n\pi}, \quad \xi_i \approx \frac{z_i}{\bar{z}_N}\bar{\xi}_N. \tag{24}$$

We can therefore consider an energy minimisation purely in terms of the variable $\bar{\xi}_N$, and the other total half-wavelengths and half-amplitudes can be derived from the resulting value.

3.2. Minimisation of wrinkle energy

Using the assumed wrinkle form in Eq. (19), and the curvature and arc length approximations of Eqs. (15) and (16), each of the energies defined at the start of Section 3 can be expressed as simplified algebraic expressions. The consolidation deviation energy, defined in Eq. (12), is given by

$$U_{\mathrm{C}}\left(w_N\right) \approx \frac{2C\left(H^0-H^*\right)}{\left(H^0\right)^2}\int_0^{\xi_N}\left(\left(A_N + A_N\cos\left(\frac{n\pi s}{\xi_N}\right)\right)^2\right) ds \tag{25}$$

$$= \frac{3C\left(H^0-H^*\right)}{\left(H^0\right)^2}\left(\frac{z_N}{\bar{z}_N}\right)^3\bar{A}_N^2\bar{\xi}_N. \tag{26}$$

The bending energy from Eq. (14) can be expressed as

$$U_{\mathrm{B}}\left(\bar{w}_i\right) \approx \frac{D_i\bar{A}_i^2 n^4\pi^4}{\bar{\xi}_i^4}\int_0^{\bar{\xi}_i}\left(\cos^2\left(\frac{n\pi s}{\bar{\xi}_i}\right)\right) ds = \frac{D_i\bar{A}_i^2 n^4\pi^4}{2\bar{\xi}_i^3}, \tag{27}$$

and, observing that $K_i = 2\bar{\xi}_i$, the in-wrinkle frictional energy from Eq. (18) can be written as

$$U_{\mathrm{Fw}}\left(\bar{w}_i\right) \approx \frac{M_f\left(\bar{w}_i\right)\bar{A}_i n^2\pi^2}{\bar{\xi}_i}\int_0^{\bar{\xi}_i}\left(\left|\cos\left(\frac{n\pi s}{\bar{\xi}_i}\right)\right|\right) ds = 8M_f\left(\bar{w}_i\right)\bar{A}_i n\pi. \tag{28}$$

From Eq. (1), the total potential energy in the laminate when forming the wrinkle is therefore

$$U_1 \approx \frac{3C\left(H^0-H^*\right)}{\left(H^0\right)^2}\left(\frac{z_N}{\bar{z}_N}\right)^3\bar{A}_N^2\bar{\xi}_N + \sum_{i=1}^{N}\left(\frac{D_i\bar{A}_i^2 n^4\pi^4}{2\bar{\xi}_i^3} + 8M_f\left(\bar{w}_i\right)\bar{A}_i n\pi\right), \tag{29}$$

which can be rewritten in terms of $\bar{\xi}_N$ using Eqs. (22)–(24) to obtain

$$U_1 \approx \frac{12\bar{\Delta}_N C\left(H^0-H^*\right)}{n^2\pi^2\left(H^0\right)^2}\left(\frac{z_N}{\bar{z}_N}\right)^3\bar{\xi}_N^2 + \sum_{i=1}^{N}\left(\frac{2D_i\left(\bar{z}_N\right)^2\bar{\Delta}_i n^2\pi^2}{\left(\bar{z}_i\right)^2\bar{\xi}_N^2} + 16M_f\left(\bar{w}_i\right)\left(\frac{\bar{z}_i}{\bar{z}_N}\right)\sqrt{\bar{\xi}_N\bar{\Delta}_N}\right). \tag{30}$$

The total potential energy is minimised with respect to $\bar{\xi}_N$ when $\frac{\partial U_1}{\partial\bar{\xi}_N} = 0$. That is, the most energetically favourable top ply total half-wavelength is a solution to

$$\frac{6\bar{\Delta}_N C\left(H^0-H^*\right)}{n^2\pi^2\left(H^0\right)^2}\left(\frac{z_N}{\bar{z}_N}\right)^3\bar{\xi}_N^4 - \left(\bar{z}_N\right)^2 n^2\pi^2\sum_{i=1}^{N}\left(\frac{D_i\bar{\Delta}_i}{\left(\bar{z}_i\right)^2}\right) + \frac{2\sqrt{\bar{\Delta}_N}}{\bar{z}_N}\sum_{i=1}^{N}\left(\bar{z}_i M_f\left(\bar{w}_i\right)\right)\bar{\xi}_N^{5/2} = 0. \tag{31}$$

The total half-wavelength $\bar{\xi}_N$ of the wrinkle is found as the smallest real positive root of Eq. (31). Eq. (22) then provides the associated half-amplitude $\bar{A}_N$, and Eqs. (20) and (23) allow us to find all the other total half-wavelengths and half-amplitudes. The individual half-wavelengths can then be recovered by dividing the total half-wavelengths by the number of wrinkles n.

4. Predicting wrinkling

The amplitudes and wavelengths resulting from the calculation described in Section 3 give the most energetically favourable profile for n grouped wrinkles if they were to form and persist. Determining when this is the case is the subject of the present section. We consider the second energy introduced in Section 2.2, given by Eq. (2), and the associated scaling factor.

The only term from Eq. (2) yet to be determined is the in-plane frictional energy, which accounts for the inter-ply slip occurring external to any wrinkling. A simple Coulomb friction model is considered, however, we discuss the assumptions under which this is applicable and the extension to more general models in Section 6. The total contact length $\hat{L}_i$, over which the friction is experienced, is introduced as separate from the part length L because, in general, the two do not coincide due to the ply orientations. For adjacent plies of orientations θ_i and θ_{i+1}, we have

$$\hat{L}_i = \max\left(\hat{\ell}_i, \hat{\ell}_{i+1}\right), \tag{32}$$

where

$$\hat{\ell}_j = \begin{cases} \frac{L}{\cos\theta_j}, & \left|\theta_j\right| \le \tan^{-1}\left(\frac{W}{L}\right), \\ \frac{W}{\left|\sin\theta_j\right|}, & \tan^{-1}\left(\frac{W}{L}\right) < \left|\theta_j\right| \le \frac{\pi}{2}. \end{cases} \tag{33}$$

The in-plane frictional energy is dependent on the compatibility of neighbouring plies, as discussed in Section 2.3, and can be expressed as

$$U_{\mathrm{F_P}}\left(w_i\right) = \left|\Delta_i^U - \Delta_{i+1}^L\right| \hat{L}_i \mu_i q. \tag{34}$$

Recalling Eq. (3), it is ultimately the ratio of this frictional term to the other parts of the energy which determines whether wrinkling is predicted to occur in the final part or not. Turning our attention to the assumed wrinkle profile from Section 3, and substituting for each component of the energy using Eqs. (26), (27), (28), and (34) as appropriate, we can explicitly give an approximation for the scaling factor as

$$\lambda \approx \frac{\frac{3C\left(H^0-H^*\right)}{\left(H^0\right)^2}\left(\frac{z_N}{\bar{z}_N}\right)^3 \bar{A}_N^2 \bar{\xi}_N + \sum_{i=1}^{N}\left(\frac{D_i \bar{A}_i^2 n^4 \pi^4}{2\bar{\xi}_i^3} - 8M_f\left(\bar{w}_i\right)\bar{A}_i n\pi\right)}{\sum_{i=1}^{N-1}\left(\left|\Delta_i^U - \Delta_{i+1}^L\right| \hat{L}_i \mu_i q\right)}. \tag{35}$$

We reiterate that wrinkling is predicted for $\lambda < 1$, which corresponds to the positive elastic terms in Eq. (2) being smaller than the frictional terms, but not for $\lambda > 1$, and a value of $\lambda = 1$ is the critical blank size on the cusp of wrinkling.

5. Analytical results and experimental validation

In this section we validate the analytical method against physical experiments and assess the formability of parts over a range of parameter values. For each test value, the top ply total half-wavelength $\bar{\xi}_N$ was calculated using Eq. (31), and the remaining half-wavelengths and corresponding half-amplitudes $\bar{A}_i$ were then determined via Eqs. (23) and (22), respectively. The scale factor λ was computed through Eq. (35) to establish the formability of the part. Analytical results were calculated for $n = 1, \ldots, 5$ wrinkles in each example, and in all cases it was found that the case of a single wrinkle minimised the total wrinkling energy U_1. The results presented in this section therefore correspond to the formation of a single wrinkle, however, the occurrence of more wrinkles is discussed in Section 6.

Our examples focus on existing experimental setups, with material parameters chosen to reflect the properties of the materials used in the experiments: Hexcel FCIM359 NCF and HTS 977-2 prepreg. The used parameter values are given in Table 1, along with the literature sources. In particular, for the NCF tests the tool geometry and blank size parameters are obtained from [21]; the bending stiffness D_0 is the mean of the positive and negative bending stiffnesses from [14]; and a short calculation is carried out to estimate the compaction stiffness C from the volume fraction results in [21]. In both the NCF and prepreg cases a default full vacuum pressure q of 0.1 N mm^{-2} is assumed, based on Scarth et al. [16], and the coefficient of friction μ for the NCF material is estimated from this and the results in [21]. For the prepreg material, the tool geometry and blank size parameters are obtained from [16], and D_0 is increased by 50% from the value stated in [22] to account roughly for a 40% increase in ply thickness and a 70% reduction in viscosity compared with AS4/8552.

The notation $\left[(X)_k\,(Y)_l\right]_m$ is used to describe a stack consisting of m repetitions of a block of l plies with orientation Y on top of a block of k plies blocks with orientation X. A lack of subscript indicates only a single copy, and the subscript S is used to imply symmetry of the stack, e.g. $\left[(0\mathrm{F})_2\,(45\mathrm{F})_2\right]_S = \left[(0\mathrm{F})_2\,(45\mathrm{F})_2\,(-45\mathrm{F})_2\,(90\mathrm{F})_2\right]$. Stacking is ordered from the tool surface to the top ply, as in Fig. 2.

Table 1
Parameter values used in the numerical examples, representative of bi-axial Hexcel FCIM359 NCF and Cytec HTS 977-2 UD prepreg materials.

Parameter	NCF (FCIM359)	UD prepreg (HTS 977-2)
μ (coefficient of friction)	0.55[a]	0.02[d]
ϕ (ramp angle, degrees)	$\tan^{-1}(0.06)$[a]	$\tan^{-1}(0.05)$[b]
t^* (consolidated ply thickness, mm)	0.40[a]	0.28[b]
C (compaction stiffness, N mm^{-2})	0.39[a]	8.0[e]
q (applied pressure, N mm^{-2})	0.10[b]	0.10[b]
D_0 (0°-ply bending stiffness, N mm)	6.8[c]	3.0[e]

References:
[a] Lawrence et al. [21].
[b] Scarth et al. [16].
[c] Yu et al. [14].
[d] Larberg and Åkermo [24].
[e] Dodwell et al. [22].

5.1. Impact of incompatible interfaces for NCF laminate

We first present verification of the model in the bi-axial context by comparing the results with experimental outcomes, motivated by the work conducted in [19]. The tests investigate the role of ply incompatibility on the appearance of wrinkles and their properties by fixing the total number of plies and their respective parameter values but varying the stacking sequence. In particular, we consider the sequences shown in Fig. 4, with increasing number of slip interfaces I.

The experimental forming trials were performed on a DDF rig at the University of Nottingham. The NCF samples used in the experiment were cut using an Assyst Bullmer XCUT automated single ply cutter to guarantee precision, repeatability and to reduce the stack preparation time, and the dimensions of each blank were 400 mm × 200 mm $(L \times W)$. A high elongation bagging film (strain to failure of approximately 500%, Yu et al. [15]), StretchLon HT-350 was used for the diaphragm material, purchased from AirTech Advanced Materials UK. The dimensions of the diaphragms were 1800 mm × 1500 mm, and each had a thickness of 0.08 mm, Yu et al. [20]. The lower diaphragm was clamped between two frames before the blank was aligned in the centre of the diaphragm, and breather fabric was placed to prevent any air becoming trapped between the two diaphragms. The upper diaphragm was then placed on top of the samples before a third frame was used to seal the arrangement, which could then be lowered over the tool using four pneumatic actuators once a vacuum had been induced between the two diaphragms. A second vacuum, induced between the lower diaphragm and the bed of the machine, provided the draping force to form the diaphragm and blank to the tool geometry.

A Creaform SilverSeries HandyScan laser scanner and VX Elements software was used to digitise the preforms in-situ on the diaphragm former. Each scan produced data in the form of a 3D point cloud, which was then processed using MATLAB to extract the conformity of the preform to the tool, Lawrence et al. [19].

In Fig. 4 the plots of surface deformation from the experiments are compared with analytical results generated using the presented model. They show good qualitative agreement with the physical experiments, in which no significant wrinkling was observed for one and two slip interfaces ($I = 1$ and $I = 2$) but wrinkling was seen for more than three interfaces. Fig. 4(c) shows that non-zero wrinkle amplitudes are observed for experimental trials with $I > 1$, however, significant wrinkling is seen for more than three slip interfaces ($I > 3$). This is in good qualitative agreement with the analytical results where we note, referring to Fig. 4(b), that the cases of both two and three slip interfaces carry greater uncertainty as they are close to the critical value for predicting wrinkling. Despite not being an exact fit, the predicted wrinkle amplitudes are on the same order of magnitude as those seen

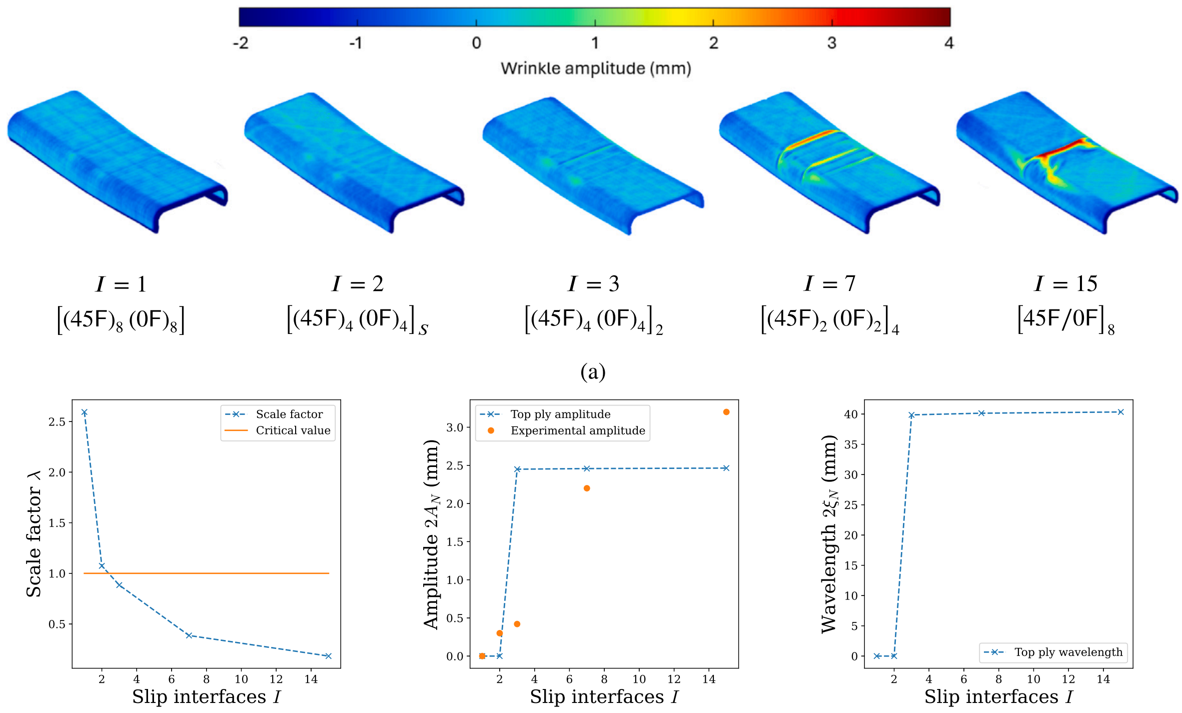

(a)

(b) (c) (d)

Fig. 4. The (a) experimental results and (b)–(d) model output from Section 5.1, where $L = 2$ W $= 400$ mm, showing the observed maximum wrinkle amplitude and wavelength and the scale factor values for stacks with a fixed number of plies but a varying number of slip interfaces I.

experimentally, which is useful for providing designers with a rough estimate of the expected scale of wrinkling. Potential explanations for the observed differences are discussed in Section 6.

5.2. Formability dependence on number of NCF plies

With our second example we aim to demonstrate the use case of the model as a first-step design tool. We assess the formability of a part with the NCF parameters detailed in Table 1 for various numbers of plies. In particular, for this test case a fixed ply length and width of 100 mm was chosen, and the stack compositions $[45F/0F]_m$, for $m = 1, 2, \ldots, 8$, were examined.

The evolution of the energies as the number of plies are varied is shown in Fig. 5, along with the associated wrinkle amplitudes and wavelengths. In this case, wrinkling occurs for 10 or more plies, and an approximately linear trend in the wrinkle amplitude and wavelength can be observed as the number of plies increases. We thus highlight the potential for the presented method as a means of determining promising laminate stacking sequences and eliminating those which show a propensity for defects from future detailed simulation and experimental trials, reducing prototyping time and costs for manufacturers.

5.3. Ply length effect for UD prepreg

In the final example we investigate the performance of the model in the case of UD prepreg plies and compare the results to the findings of Scarth et al. [16], which demonstrated the ply length effect in 6 m long spars. In this phenomenon, the inclusion of plies with fibre directions aligned with the principal direction of the tool geometry exhibit wrinkling when the part being formed is particularly large, even if the stacking sequence has a high compatibility index ($C_{\max}$).

The stacking sequences considered and the associated analytical results are shown in Table 2, where for comparison we have included the predicted maximum amplitude and wavelength for all stacking sequences even if wrinkling is not predicted ($\lambda > 1$). The model is in good agreement with the outcome of the physical experiments (see Fig. 6), predicting that the laminate featuring plies with non-standard orientations (avoiding the length effect) is formable and those laminates which contain 6 m-long 0° plies exhibit wrinkling. Attention is drawn to the difference in formability of the laminates despite the similarity of the predicted wrinkle amplitudes and wavelengths for each of the three stacking sequences. The present model demonstrates that wrinkle amplitude and wavelength are mainly driven by design parameters such as the number of plies and the tool geometry (which are fixed for all the considered stacking sequences), whereas the determining factor in wrinkle occurrence is the length effect, which is captured here through the in-plane frictional energy of Eq. (34).

Table 2
Analytical results for the UD prepreg case of Section 5.3, showing the predicted maximum wrinkle amplitudes and wavelengths (in mm) along with the associated scaling factor indicating whether wrinkling is expected. The three stacking sequences correspond to laminates A, B, and C, respectively, in [16].

Stacking sequence	Max. amplitude $2A_N$ (mm)	Max. wavelength $2\xi_N$ (mm)	Scaling factor λ
$[\pm 45/90/0/\mp 45]_{2S}$	2.4	21	0.94
$[(\pm 45)_4\,(0/90)_2]_S$	2.4	21	0.91
$[(27/-63)_3\,(-27/63)_3]_S$	2.5	23	3.2

6. Discussion

There are several simplifying assumptions in the analysis that should be noted. The use of a Coulomb-type frictional model neglects the contribution of the uncured resin in prepreg material and can subsequently overestimate shear stresses, Larberg and Åkermo [24]. A viscoelastic model, such as the one introduced in [25], which features a temperature-dependent viscous component and a pressure-dependent component, is more appropriate to capture the transient and nonlinear nature of the frictional response in UD prepreg material, see [26]. Our

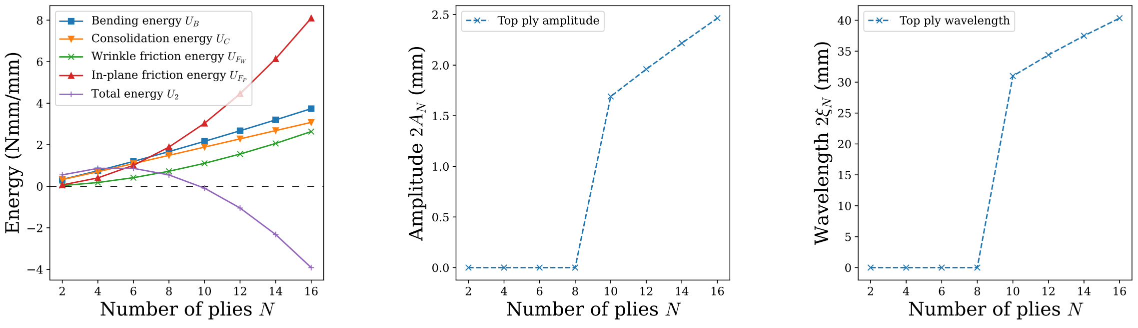

(a) (b) (c)

Fig. 5. The analytical results from Section 5.2, for a laminate with stacking sequence $[45F/0F]_m$, where $m = 1, 2, \ldots, 8$, and $L = W = 100$ mm, showing the (a) system energies, (b) maximum wrinkle amplitude, and (c) wavelength as functions of the number of plies.

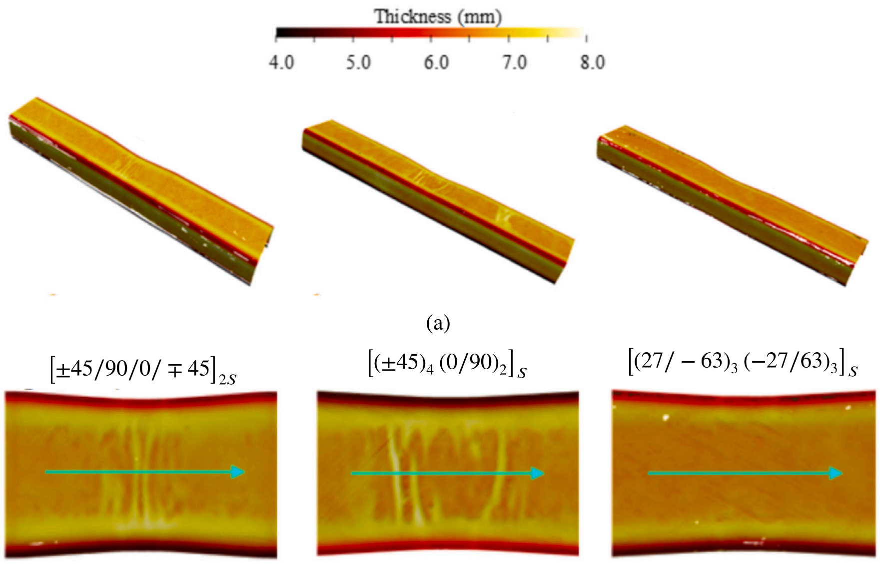

(b)

Fig. 6. Experimental thickness maps of the three laminates in Section 5.3, showing the central 1 m sections of the spars (a) and focused views of the central recesses (b), measured from metrology data taken at the post-forming, pre-cure stage, Scarth et al. [16]. Wrinkles are seen in both laminates composed of standard-angle plies, but no wrinkles are observed in the laminate containing plies of non-standard angles.

model is valid in the case of dry fibres, such as with NCF, and at slow forming rates, where viscous friction is not dominant. The parametric values listed in Table 1 also have a degree of uncertainty; for example, the degree to which full vacuum is achieved and the transient nature of the forming problem are not modelled; neither do we capture nonlinear effects such as those associated with consolidation energy. We also note that the assumed wrinkle shape and the single degree of freedom (bookending angle) which generates it are simplifications of the wrinkle shape and the kinematics involved in forming. Double curvature will also induce significant through-thickness variation of in-plane shear deformation, and this effect is not included in the model.

Figs. 4 and 6 demonstrate that multiple wrinkles can be observed experimentally in both the NCF and UD prepreg cases. With the analytical results shown in Tables 3 and 4, we now discuss the cases in which more than one wrinkle occurs in Section 5.1 with $I = 7$ and the first stacking sequence in Section 5.3, respectively. Only results up to and including a total wrinkling length exceeding 100 mm are included since this is the length of the central recess in which wrinkles are observed. The values in the tables suggest that laminates with more wrinkles of smaller amplitude are less formable, having a smaller scaling factor λ, but have greater associated wrinkling energies and so are not expected to be observed. Clearly this is not always the case, and simplifications mean that, whilst wrinkling was correctly predicted, the analytical model does not accurately reflect all physical behaviours.

Referring to Eq. (29), the bending energy dominates the other terms as n increases, and the total wrinkling energy increase is exacerbated by large values for the coefficient of friction μ and bending stiffness D_0. This is particularly the case with the NCF material, which has much larger values for μ and D_0 than the UD prepreg material. For the latter, we note that the total wrinkling energies in Table 4 are in very close proximity, and so the predicted occurrence of multiple wrinkles in the UD prepreg material is more likely.

Some of the experimentally-observed wrinkles show larger or smaller amplitudes than are predicted by the model. The $I = 15$ case of Fig. 4(a) shows a wrinkle with amplitude over 25% greater than predicted in Fig. 4(c), whereas in the $I = 3$ case the experimental amplitude is significantly smaller than predicted. It is possible that slip between the tool and the laminate induces end shortening over the full laminate thickness and contributes to wrinkling of all plies, including those on the tool surface. This effect, not considered in the model, would amplify the wrinkle. Fig. 4(b) shows that the $I = 3$ case is close to being formable, and here it is possible that significant dissipation of the wrinkle occurred before full vacuum was achieved. Anomalies

Table 3
Multi-wrinkle results for $n = 1, 2, 3$ from Section 5.1, with $I = 7$ slip interfaces.

Number of wrinkles (n)	Total max. wavelength $2\xi_N$ (mm)	Max. amplitude $2A_N$ (mm)	Individual max. wavelength $2\hat{\xi}_N$ (mm)	Total wrinkling energy U_1 (N mm/mm)	Scaling factor λ
1	40.1	2.46	40.1	9.38	0.386
2	78.7	1.72	39.4	10.5	0.290
3	116	1.40	38.8	11.3	0.219

Table 4
Multi-wrinkle results for $n = 1, \ldots, 5$ for the first stacking sequence (laminate A in [16]) from Section 5.3.

Number of wrinkles (n)	Total max. wavelength $2\xi_N$ (mm)	Max. amplitude $2A_N$ (mm)	Individual max. wavelength $2\hat{\xi}_N$ (mm)	Total wrinkling energy U_1 (N mm/mm)	Scaling factor λ
1	21.6	2.40	21.6	12.0	0.942
2	43.2	1.69	21.6	12.1	0.935
3	64.7	1.38	21.6	12.1	0.930
4	86.2	1.20	21.6	12.2	0.926
5	108	1.07	21.5	12.2	0.922

in the experimental scan data caused by stitching and fabric bridging could also contribute to the difference in amplitudes.

The model accounts for wrinkling that maximises on the surface of the part (the outer mould line). It is also possible, though not represented here, that curvature in the opposite direction (convex rather than concave), for example during forming of the C-spar corner radii, maximises compression in plies closest to the tool (the inner mould line). The effects of post-forming consolidation and curing have not been considered as the approach assumes the key driver of out-of-plane wrinkling is the restraint of inter-ply slip due to frictional effects. Only bookend generated by the geometry of the tool is incorporated, however, the model could be extended to account for additional bookend arising, for example, during consolidation. Other factors which could force the blank to shear, such as a reduction in the cross-sectional area of the tool in the central recess or the blank being larger than the tool, are also not accounted for by the one-dimensional model reduction approach adopted. The model does not consider the behaviour of the resin in prepreg systems and, despite the agreement with experimental results, is only able to assess the formability of the laminate, with no indication of the quality of the final part.

The energy minimisation of Eq. (31) determines the ratio of wavelength to amplitude assuming small deformation theory. The assumptions made would not be valid for the highly-localised (pinch point) case leading to large amplitude, small wavelength wrinkles. The method is therefore applicable only to wrinkles which have a small amplitude relative to their wavelength. Predicting such wrinkles has been limited here to a range of C-spar geometries parameterised only by the involved ramp angle. The modelling of wrinkling behaviour on more general (non-symmetric) geometries could be examined in future work, alongside a new experimental test programme.

For the above reasons we emphasise the scope of the method, which is to facilitate fast preliminary design of parts and production processes prior to detailed finite element analysis and expensive production trials. Despite the highlighted limitations, the two-stage analytical model we present can successfully predict the three cases for which wrinkling is absent and the five cases where it occurs in physical forming experiments for multi-ply NCF and UD prepreg material. We note that such experiments require significant investment in time and materials; for example, each of the three experiments in Section 5.3 required over 20 kg (50 m^2) of UD prepreg material.

7. Conclusions

A novel analytical model has been presented that can predict the conditions which enable wrinkle-free Double Diaphragm Forming of a symmetric part with double curvature. The method is suitable for use in preliminary design of laminates and production conditions to ensure formability, provided that the frictional, bending, and consolidation properties of the material are known as well as the stacking sequence, bookending angle, and the extent of operational vacuum. The method enables rapid mechanics-based assessment of formability for both unidirectional prepreg (UD prepreg) and dry Non-Crimped Fabric (NCF) materials, which was previously unachievable by existing methods such as finite element analysis. Results compare well with experimental forming trials for both NCF and UD prepreg material showing that formability can be improved by reducing the friction between layers. This is achieved by either reducing the number of sliding interfaces between plies with incompatible fibre orientations or by reducing the frictional fibre length using non-standard ply angles. The speed of the approach improves the capability of iterating through design parameters and allows designers to quickly reject infeasible geometries or ply stacking sequences, paving the way for zero-defect manufacture of laminated parts at high rates of production with more layers able to be formed simultaneously without scrappage or concession of high-value composite parts.

CRediT authorship contribution statement

Alex Trenam: Writing – original draft, Visualization, Software, Methodology, Investigation, Formal analysis, Conceptualization. **Chrysoula Aza:** Writing – review & editing, Methodology, Investigation, Conceptualization. **Christian Jones:** Writing – review & editing, Methodology, Investigation, Conceptualization. **Guy Lawrence:** Writing – review & editing, Visualization, Investigation, Formal analysis. **Lee Harper:** Writing – review & editing, Supervision. **Andrew Rhead:** Writing – review & editing, Supervision, Methodology, Conceptualization. **Evripides G. Loukaides:** Writing – review & editing, Supervision, Methodology, Conceptualization. **Richard Butler:** Writing – review & editing, Supervision, Methodology, Funding acquisition, Conceptualization.

Declaration of competing interest

The authors declare that they have no known competing financial interests or personal relationships that could have appeared to influence the work reported in this paper.

Data availability

Data will be made available on request.

Acknowledgements

This work was funded by Design, Simulation Tools and Process Improvements for NCF Preforming (NCForm), UK, a Core project under the EPSRC Future Composites Manufacturing Research Hub, UK (EP/P006701/1). NCForm is led by Professor Michael Sutcliffe at the University of Cambridge, and we are particularly grateful for his many helpful contributions. Alex Trenam is supported by NCForm, UK and by a Ph.D. studentship from the EPSRC Centre for Doctoral Training in Advanced Automotive Propulsion Systems, UK (EP/S023364/1). Access to the 3D laser scanner was kindly provided by the HV-Command EPSRC Strategic Equipment Grant (EP/T006420/1), UK.

References

[1] Chen S, McGregor OPL, Harper LT, Endruweit A, Warrior NA. Optimisation of local in-plane constraining forces in double diaphragm forming. Compos Struct 2018;201:570–81. http://dx.doi.org/10.1016/J.COMPSTRUCT.2018.06.062.

[2] Chen S, Joesbury AM, Yu F, Harper LT, Warrior NA. Optimisation of intra-ply stitch removal for improved formability of biaxial non-crimp fabrics. Composites B 2022;229:109464. http://dx.doi.org/10.1016/J.COMPOSITESB.2021.109464.

[3] Yu F, Chen S, Lawrence GD, Warrior NA, Harper LT. A global-to-local sub modelling approach to investigate the effect of lubrication during double diaphragm forming of multi-ply biaxial non-crimp fabric preforms. Composites B 2023;254:110590. http://dx.doi.org/10.1016/J.COMPOSITESB.2023.110590.

[4] Jagpal R, Evangelou E, Butler R, Loukaides EG. Preforming of non-crimp fabrics with distributed magnetic clamping and Bayesian optimisation. J Compos Mater 2022;56:2835–54. http://dx.doi.org/10.1177/00219983221103637, URL http://journals.sagepub.com/doi/10.1177/00219983221103637.

[5] Allaoui S, Cellard C, Hivet G. Effect of inter-ply sliding on the quality of multilayer interlock dry fabric preforms. Composites A 2015;68:336–45. http://dx.doi.org/10.1016/J.COMPOSITESA.2014.10.017.

[6] Nezami FN, Gereke T, Cherif C. Analyses of interaction mechanisms during forming of multilayer carbon woven fabrics for composite applications. Composites A 2016;84:406–16. http://dx.doi.org/10.1016/J.COMPOSITESA.2016.02.023.

[7] Mukhopadhyay S, Jones MI, Hallett SR. Compressive failure of laminates containing an embedded wrinkle; experimental and numerical study. Composites A 2015;73:132–42. http://dx.doi.org/10.1016/J.COMPOSITESA.2015.03.012.

[8] Mukhopadhyay S, Jones MI, Hallett SR. Tensile failure of laminates containing an embedded wrinkle; numerical and experimental study. Composites A 2015;77:219–28. http://dx.doi.org/10.1016/J.COMPOSITESA.2015.07.007.

[9] Johnson KJ, Butler R, Loukaides EG, Scarth C, Rhead AT. Stacking sequence selection for defect-free forming of uni-directional ply laminates. Compos Sci Technol 2019;171:34–43. http://dx.doi.org/10.1016/j.compscitech.2018.11.048.

[10] Belnoue JPH, Nixon-Pearson O, Ivanov D, Hallett S. A novel hyper-viscoelastic model for consolidation of toughened prepregs under processing conditions. Mech Mater 2016;97:118–34. http://dx.doi.org/10.1016/j.mechmat.2016.02.019, URL https://www.sciencedirect.com/science/article/pii/S0167663616000508.

[11] Belnoue JPH, Valverde MA, Onoufriou M, Sun XR, Ivanov DS, Hallett SR. On the physical relevance of power law-based equations to describe the compaction behaviour of resin infused fibrous materials. Int J Mech Sci 2021;199:106425. http://dx.doi.org/10.1016/j.ijmecsci.2021.106425, URL https://www.sciencedirect.com/science/article/pii/S0020740321001600.

[12] Schirmaier FJ, Dörr D, Henning F, Kärger L. A macroscopic approach to simulate the forming behaviour of stitched unidirectional non-crimp fabrics (UD-NCF). Composites A 2017;102:322–35. http://dx.doi.org/10.1016/J.COMPOSITESA.2017.08.009.

[13] Liang B, Colmars J, Boisse P. A shell formulation for fibrous reinforcement forming simulations. Composites A 2017;100:81–96. http://dx.doi.org/10.1016/j.compositesa.2017.04.024.

[14] Yu F, Chen S, Viisainen JV, Sutcliffe MPF, Harper LT, Warrior NA. A macroscale finite element approach for simulating the bending behaviour of biaxial fabrics. Compos Sci Technol 2020;191:108078. http://dx.doi.org/10.1016/j.compscitech.2020.108078.

[15] Yu F, Chen S, Harper LT, Warrior NA. Double diaphragm forming simulation using a global-to-local modelling strategy for detailed defect detection in large structures. Composites A 2021;147:106457. http://dx.doi.org/10.1016/J.COMPOSITESA.2021.106457.

[16] Scarth C, Chen Y, Aza C, Rhead AT, Butler R. Manufacture of long spars: Laminate design, experimental trials and non-destructive evaluation. Composites B 2023;255:110646. http://dx.doi.org/10.1016/j.compositesb.2023.110646, URL http://creativecommons.org/licenses/by/4.0/.

[17] Thompson AJ, McFarlane JR, Belnoue JP-H, Hallett SR. Numerical modelling of compaction induced defects in thick 2D textile composites. Mater Des 2020;196:109088. http://dx.doi.org/10.1016/j.matdes.2020.109088, URL https://www.sciencedirect.com/science/article/pii/S0264127520306237.

[18] Rashidi A, Belnoue JP-H, Thompson AJ, Hallett SR, Milani AS. Consolidation-driven wrinkling in carbon/epoxy woven fabric prepregs: An experimental and numerical study. Composites A 2021;143:106298. http://dx.doi.org/10.1016/j.compositesa.2021.106298, URL https://www.sciencedirect.com/science/article/pii/S1359835X21000282.

[19] Lawrence GD, Chen S, Warrior NA, Harper LT. Preforming of multi-ply non-crimp fabric laminates using double diaphragm forming. In: Twenty-third international conference on composite materials (ICCM23), Belfast. Belfast; 2023.

[20] Yu F, Chen S, Harper LT, Warrior NA. Investigation into the effects of inter-ply sliding during double diaphragm forming for multi-layered biaxial non-crimp fabrics. Composites A 2021;150:106611. http://dx.doi.org/10.1016/j.compositesa.2021.106611.

[21] Lawrence GD, Chen S, Warrior NA, Harper LT. The influence of inter-ply friction during double-diaphragm forming of biaxial NCFs. Composites A 2023;167:107426. http://dx.doi.org/10.1016/j.compositesa.2023.107426.

[22] Dodwell TJ, Butler R, Hunt GW. Out-of-plane ply wrinkling defects during consolidation over an external radius. Compos Sci Technol 2014;105:151–9. http://dx.doi.org/10.1016/j.compscitech.2014.10.007.

[23] Krenchel H. Fibre reinforcement: theoretical and practical investigations of the elasticity and strength of fibre-reinforced materials. Copenhagen: Akademisk Forlag; 1964.

[24] Larberg YR, Åkermo M. On the interply friction of different generations of carbon/epoxy prepreg systems. Composites A 2011;42:1067–74. http://dx.doi.org/10.1016/j.compositesa.2011.04.010, URL https://linkinghub.elsevier.com/retrieve/pii/S1359835X11001163.

[25] Pierik E, Grouve W, Wijskamp S, Akkerman R. Modeling the effect of temperature and pressure on the peak and steady-state ply–ply friction response for UD C/PAEK tapes. Composites A 2023;173:107671. http://dx.doi.org/10.1016/j.compositesa.2023.107671, URL https://www.sciencedirect.com/science/article/pii/S1359835X23002476.

[26] Erland S, Dodwell TJ, Butler R. Characterisation of inter-ply shear in uncured carbon fibre prepreg. Composites A 2015;77:210–8. http://dx.doi.org/10.1016/J.COMPOSITESA.2015.07.008.